

## Research article

---

# The Effect of Annealing Treatment on WO<sub>3</sub> Thin Film Prepared by Reactive DC Magnetron Sputtering for Photo-electrochemical Water Splitting Application

Tienthong Yuangkaew<sup>1</sup>, Chatchai Ponchiyo<sup>2</sup>, Peerapong Nuchuay<sup>3</sup>, Viyapol Patthanasettakul<sup>4</sup>, Pitak Eiamchai<sup>4</sup>, Noppadon Nuntawong<sup>4</sup>, Mati Horprathum<sup>4</sup> and Saksorn Limwichean<sup>4\*</sup>

<sup>1</sup>Department of Electrical Engineering, Faculty of Engineer, Rajamangala University of Technology Isan, Khon Kaen Campus, Khon Kaen, Thailand

<sup>2</sup>Department of Chemistry, Faculty of Science and Technology, Rajamangala University of Technology Thanyaburi, Pathum Thani, Thailand

<sup>3</sup>Program of Industrial Electrical Technology, Faculty of Science and Technology, Suratthani Rajabhat University, Surat Thani, Thailand

<sup>4</sup>National Electronics and Computer Technology Center (NECTEC), National Science and Technology Development Agency, Pathum Thani, Thailand

Received: 3 October 2022, Revised: 7 November 2022, Accepted: 28 March 2023

DOI: 10.55003/cast.2023.06.23.010

## Abstract

### Keywords

WO<sub>3</sub> thin film;  
DC magnetron sputtering;  
photoelectrochemical water splitting

In this work, WO<sub>3</sub> thin films were fabricated by reactive DC magnetron sputtering, and then thermally annealed at 400°C for 2 h under air, low vacuum and high vacuum. After the annealing treatments, the morphology and crystallinity of the WO<sub>3</sub> thin films were observed using FE-SEM, GI-XRD and Raman spectroscopy. The optical properties were analyzed by UV-Vis spectroscopy. The results showed the decrease of film thickness under different annealing conditions. In addition, the annealing conditions also affected the crystalline structure at diffraction planes (200) and (002). The transmittance of the WO<sub>3</sub> thin films revealed that the annealing treatment at high vacuum led to lower transparency. Furthermore, the WO<sub>3</sub> thin film annealed under air produced the highest PEC efficiency. Therefore, this approach offers an alternative strategy for photoelectrochemical (PEC) water splitting application.

---

\*Corresponding author: Tel.: (+66) 25646900 Ext.2700

E-mail: saksorn.limwichean@nectec.or.th

## 1. Introduction

The development of metal oxide semiconductors for photoelectrochemical water splitting has led to new potential application in H<sub>2</sub> production [1, 2]. To obtain the efficient photoanode, light absorption capability and charge separation must be realized. The generation of electron-hole pairs depends on the light absorption capability. Narrow band gap energy materials are also required. To generate a photoelectrochemical reaction, a separation and migration of electrons and holes are needed to overcome the recombination process.

Among the metal oxide materials, WO<sub>3</sub> is suitable for use as a photoanode because it has a narrow band gap energy and superior charge transport properties. WO<sub>3</sub> has superior potential to be used as a photocatalytic material due to its low cost, environment friendliness, and stability in acidic and oxidative conditions [3]. In addition, it possesses a narrow band gap energy (2.5-2.8 eV) making it suitable for visible light utilizations [4]. The mechanism of the photocatalytic activity of WO<sub>3</sub> depends on the separation and transfer of photo-generated charge carriers. Many strategies have been proposed. The reactive DC magnetron sputtering technique provides a uniform distribution of sputtered materials and can produce good adhesion between sputtered materials and substrates [5, 6]. Annealing treatments are widely used to improve WO<sub>3</sub> properties. It was observed that high annealing temperature increased the PEC performance of WO<sub>3</sub> nanosheet/nanorods [7]. Moreover, varying the conditions of annealing can lead to a range of electronic and optical properties of WO<sub>3</sub>. Air annealing of samples provides a maximum photocurrent density that is significantly higher than those of O<sub>2</sub> and H<sub>2</sub> annealed samples [8]. The WO<sub>3</sub> film that forms in vacuum annealing has the sub-stoichiometric formula of WO<sub>3-x</sub>. Air-annealed film has a lower light absorption in the visible region compared with film annealed in a vacuum. Furthermore, both air and vacuum annealing have substantial effects on the photoelectrochemical activity of WO<sub>3</sub> films [9]. The annealing ambient has a strong influence on the morphology of film surface, phase transition and crystal structure [10]. Therefore, an exhaustive examination on the effects of annealing treatment conditions on the PEC performance of WO<sub>3</sub> thin films were performed.

In this work, direct current magnetron sputtering technique was used to fabricate WO<sub>3</sub> thin film. High vacuum, low vacuum and air annealing of prepared samples were considered in aspect of photoelectrochemical water splitting. The obtained WO<sub>3</sub> photoanodes were examined on the corresponding to morphology, optical properties, and photocurrent response. The thickness of their nanostructure WO<sub>3</sub> layer could be fluctuate due to changes in the annealing conditions. The crystallinity and the presence of oxygen vacancies were also investigated because these properties are important factors in the analysis of PEC water splitting performance. Finally, the photocurrent response of annealed photoanodes were measured and discussed. The optimized photo-response behavior of the sample could be promising candidates with high performance in PEC water splitting applications.

## 2. Materials and Methods

### 2.1 Fabrication of WO<sub>3</sub> thin films

The WO<sub>3</sub> thin films were fabricated by reactive direct current magnetron sputtering technique as described in our previous work [5]. The sputtered WO<sub>3</sub> particles were deposited on glass slide substrates, bare silicon wafer substrates, and on transparent conductive glass slides (ITO) substrates with sheet resistance of 12 Ohm/sq. Their optical transmittance was measured on glass slide substrate samples, and bare silicon wafers were used for thin-film characterization. Photocurrent response was evaluated on ITO coated glass slide substrate samples. All substrates were

successively sonicated with acetone, isopropanol. Then, the substrates were rinsed in deionized water. Finally, the substrates were blown with  $N_2$  before loading with the various substrates onto sample holders in sputtering chamber. A high pure quality tungsten disc (99.995%, from Kurt J. Lesker) with diameter of 3 inches was used as the sputtering target. The pre-sputtering process was operated at 100 W DC power for 3 min in argon atmosphere with base pressure of  $5.0 \times 10^{-6}$  mbar. During the sputtering deposition, the tungsten target was sputtered in a mixture of 99.999% oxygen and 99.999% argon at constant feed rates of 80 and 100 sccm, respectively. The sputtering process was supplied at DC power of 75 W to generate plasma discharge. The operating pressure was  $3.5 \times 10^{-3}$  mbar. The substrates were rotated at 10 rpm with the deposition time of 30 min. Finally, the obtained samples were annealed in air, low vacuum ( $5 \times 10^{-3}$  mbar) and high vacuum ( $5 \times 10^{-6}$  mbar) at 400°C for 2 h.

## 2.2 Characterization

A Hitachi SU8030 field emission electron microscope (FE-SEM) was used to observed the physical morphology and the film thickness. The crystallographic analysis of the post annealing samples was performed with a glancing-incident X-ray diffraction (GIXRD, Rigaku) using a monochromatized Cu  $K\alpha$  radiation source at 50 kV supply voltage and 300 mA current. The XRD measurements were set at 0.02° steps from 20° to 70° and scanning speed of 3°/min. The optical transmittance was measured by an Agilent Cary 7000 UV–Vis–NIR spectrophotometer with the wavelength ranging from 300 to 2000 nm. In addition, Raman scattering spectra was obtained on a confocal Raman microscope (Ranishaw inVia Reflex) for analysis of crystallinity of the  $WO_3$ . The Raman spectra measurement was recorded with laser excitation at 532 nm and 0.5 mW laser power. The exposure time was set at 20 s. The water photo-oxidation performances of obtained  $WO_3$  thin-films were measured with a three-electrode cell configuration in 0.5 M  $Na_2SO_4$  aqueous solution, as shown in Figure 1. The applied potential was controlled at 1.0 V vs. Ag/AgCl on a PAR-VersaSTAT3 voltammetry analyzer under chopped visible light illumination. Prepared  $WO_3$  thin film deposited on ITO coated glass slide was used as working electrode. Pt wire was used as counter electrode. The reference electrode was Ag/AgCl (in 3 M NaCl, Bioanalytical System, Inc.).

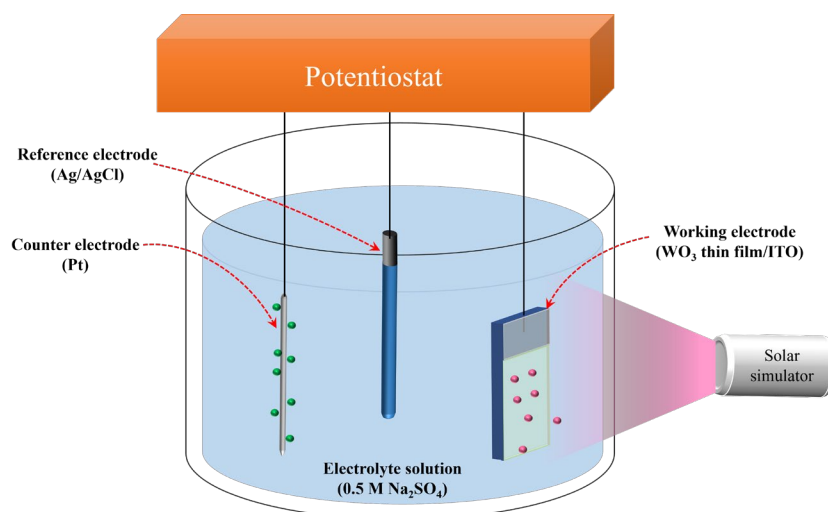


**Figure 1.** Photoelectrochemical measurement setup

### 3. Results and Discussion

Figure 2(a) showed the surface morphology and cross section FE-SEM images of tungsten oxide thin films at various ambient annealing conditions. After annealing under air and low vacuum, the  $\text{WO}_3$  grain boundaries were more obvious compared to those of as-deposited  $\text{WO}_3$  thin film. Moreover, the grain morphology was slightly changed after annealing under high vacuum. The cross-sectional  $\text{WO}_3$  thin film appeared to be flat and dense. The SEM images show that annealing conditions had an effect on the thickness of  $\text{WO}_3$  thin film, as shown in Figure 2(b). The annealing treatments produced greater film thickness in the following order: high vacuum, low vacuum and air. For the air annealing condition, the thinnest film was produced. The thickness of the  $\text{WO}_3$  thin film layer was measured to be approximately 410 nm. Low vacuum annealed  $\text{WO}_3$  film and high vacuum annealed  $\text{WO}_3$  film exhibited the thicknesses of 440 and 460 nm, respectively. Our results showed a similar trend to those in the literature [10]. The lowest thickness of the air-annealed sample was probably due to the formation of fully stoichiometric  $\text{WO}_3$  [9]. W–O atom pairs during phase transformation tend to become arranged in a higher-ordered crystalline structure. Under vacuum annealed conditions, the presence of sub-stoichiometric  $\text{WO}_{3-x}$  leads to formation of delocalized atoms and dangling bonds.

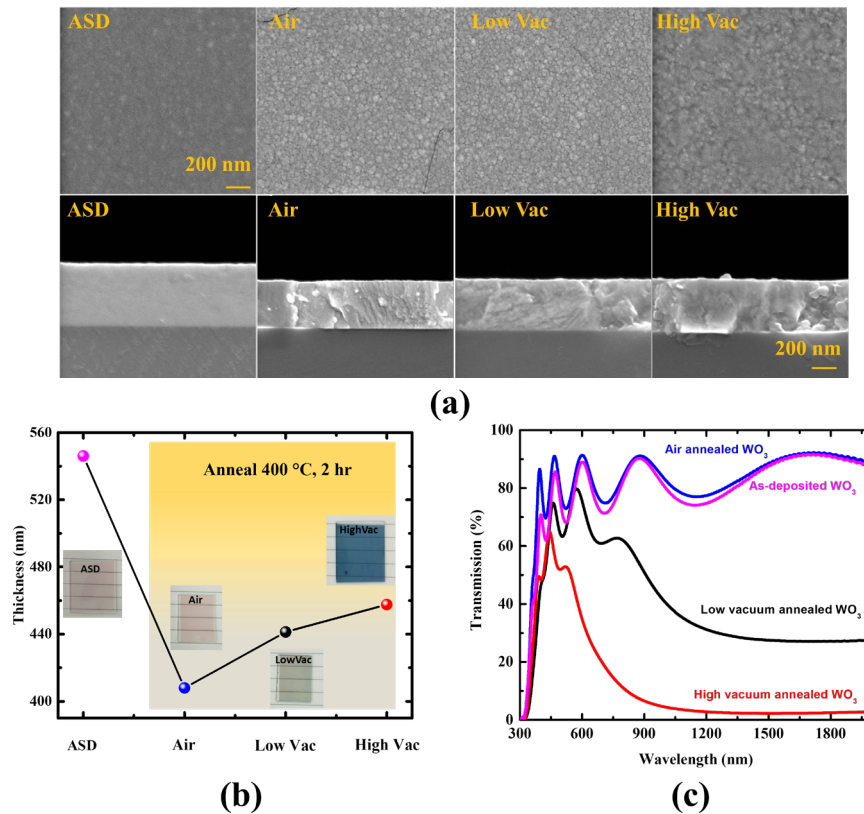


**Figure 2.** (a) Cross sectional SEM images of various annealing conditions and (b) The thickness of obtained samples and (c) The optical transmission of prepared  $\text{WO}_3$  thin film

Photographs illustrating the transparency and color of the prepared WO<sub>3</sub> thin films are shown in Figure 2(b). The color of air annealed coated film was nearly unchanged compared to that of the as-deposited WO<sub>3</sub> thin film. For low vacuum treated WO<sub>3</sub> thin film, the color of the film changed from light red to light green. Under high vacuum treatment, the color of the film became blue. Therefore, it can be observed that the thickness of WO<sub>3</sub> thin film layers affected the transition of color.

Furthermore, transmittance measurements were employed to analyze the transparency of WO<sub>3</sub> thin films. Figure 2(c) shows the transmittance spectra of the as-deposited WO<sub>3</sub> thin film and the post annealed WO<sub>3</sub> thin film. The optical interference resulting from WO<sub>3</sub> thickness layer was obviously observed. The average transmittance ( $T_{avg}$ ) of obtained samples was evaluated from the calculation of integral visible transmittance in the range of 380 to 780 nm using the following formula [11].

$$T_{avg} = \frac{\int \phi_{lum}(\lambda)T(\lambda)d(\lambda)}{\int \phi_{lum}(\lambda)d(\lambda)} \quad (1)$$

Where  $T(\lambda)$  is the transmittance at wavelength in the visible region,  $\phi_{lum}$  denotes the standard luminous efficiency function for photonic vision of human eye.

$T_{avg}$  of the as-deposited sample, air annealed sample, low vacuum annealed sample, and high vacuum annealed sample were calculated as 75.90%, 80.57%, 65.51%, and 37.80%, respectively. The highest average transmittance was obtained for the air annealed WO<sub>3</sub> thin film, probably due to the smaller film thickness. The higher transparency can be attributed to the penetration of photon particles resulting in the generation of large number of photo-excited carriers. These features then promote light harvesting applications.

The transmittance spectra can be converted to absorption coefficient for the evaluation of band gap energy. The absorption coefficient was calculated according to Velevska *et al.* [12].

$$\alpha(\nu) = \frac{1}{d} \ln \frac{1}{T} \quad (2)$$

Where  $T$  is the measured transmittance spectra and  $d$  is the film thickness.

The band gap energy was evaluated by extrapolating the linear region of Tauc plot using Tauc's equation [19].

$$\alpha(h\nu)^n = B(h\nu - E_g) \quad (3)$$

Where  $B$  is a constant,  $h\nu$  is the incident photon energy,  $E_g$  is the band gap energy, and the absorption coefficient is  $\alpha$ . The index  $n$  provides the type of electronic transitions causing the absorption. The values of  $n$  are 1/2, 2, and 2/3 for indirect allowed, direct allowed, and direct forbidden, respectively.

The calculated energy gaps of the thin films annealed under air, low vacuum and high vacuum were about 3.16, 2.78, and 2.92 eV, respectively (Figure 3). The band gap energy decreased when annealing was done in vacuum ambient compared to air annealed sample. Vacuum annealing provided more creation of oxygen vacancies. The existence of oxygen vacancies resulted from the defect state and consequently created defective band energy levels below the conduction band. This localized state increased with increasing oxygen vacancy concentration and resulted in the band gap energy becoming narrower.

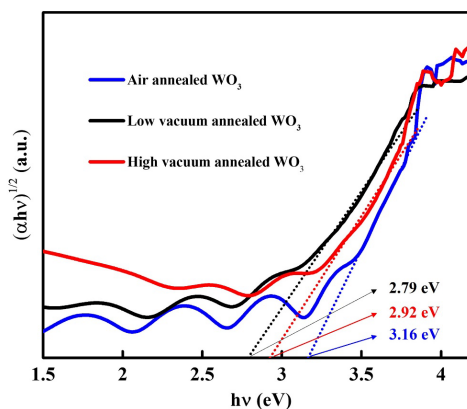


**Figure 3.** Variation of the optical band gap of  $\text{WO}_3$  thin films at different annealing conditions

Grazing incident X-ray diffraction was employed to identify the crystal structure and crystallinity of the prepared samples. The as-deposited  $\text{WO}_3$  film clearly presented amorphous structures. At air annealed  $\text{WO}_3$  thin film and low vacuum annealed  $\text{WO}_3$  thin film, monoclinic phase was detected from the XRD patterns, as shown in Figure 4(a). Several significant peaks appeared, which were the (020), (200), (112), (202), and (222) facets of JCPDS Card No. 43-1035. A narrow half-width maximum peak indicates a higher degree of crystallinity of film. For high vacuum annealed  $\text{WO}_3$  thin film, broadened peaks and diminished peaks were evidenced compared to the air annealed sample. These phenomena provided evidence of higher disordering of crystal structure. Thus, the high vacuum annealed  $\text{WO}_3$  film under a low oxygen content atmosphere also provided low crystallinity. The existence of oxygen-related crystal defects promotes the presence of oxygen vacancies. Notably, a higher proportion of XRD peaks related with the (200) plane and the (020) plane in the low vacuum annealed  $\text{WO}_3$  film were seen compared to the air annealing  $\text{WO}_3$  sample. This result indicated that low vacuum annealed  $\text{WO}_3$  preferentially grew along the [100] direction. During the PEC water splitting process, the formation of  $\text{OH}^*$  species is typically known to occur more readily on the (200) plane compared to the (002) plane [8]. Inversely, photo-assisted water oxidation occurs preferentially on the (002) plane [5, 13]. Consequently, air annealed  $\text{WO}_3$  tended to demonstrate the higher photoactivity of PEC water splitting.

Raman spectra were created to study the crystallinity of the  $\text{WO}_3$  thin films. The Raman shift is sensitive to W-O bonds in crystal structure. Hence, various annealing conditions of thin films exhibited different Raman spectra. Figure 4(b) shows the Raman spectra of the as-deposited  $\text{WO}_3$  thin film and various annealed  $\text{WO}_3$  thin films. The as-deposited  $\text{WO}_3$  thin film and high vacuum annealed  $\text{WO}_3$  thin films did not show the specific peaks of any  $\text{WO}_3$  crystal structure. The Raman spectra of the air annealed  $\text{WO}_3$  thin film significantly indicated 4 major peaks at 134, 272, 714, and 806  $\text{cm}^{-1}$ . All vibrational characteristic peaks were identified to be lattice mode (134  $\text{cm}^{-1}$ ),  $\delta(\text{O-W-O})$  bending mode (272  $\text{cm}^{-1}$ ), and  $\nu(\text{O-W-O})$  stretching mode (717 and 806  $\text{cm}^{-1}$ ) [5, 14]. These Raman peaks clearly revealed the rearrangement of crystallinity with monoclinic phase corresponding to our XRD results and other literatures [15, 16]. In the low vacuum annealing  $\text{WO}_3$  treatment, the Raman spectra band of the monoclinic phase was maintained but the characteristic peaks slightly shifted towards lower wavenumber (711  $\text{cm}^{-1}$ ), which related to the air annealed  $\text{WO}_3$  thin film. This phenomenon was caused by increased creation of oxygen vacancies [17]. Moreover, an additional Raman peak in the air annealed  $\text{WO}_3$  film at 326  $\text{cm}^{-1}$  was obviously observed and it indicated an enhancement of crystallinity compared to low vacuum annealed  $\text{WO}_3$  [18].

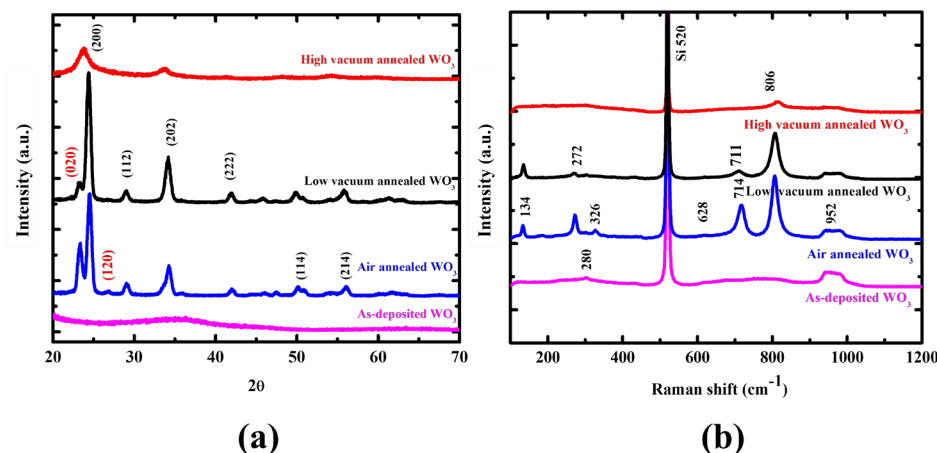


**Figure 4.** Crystal structure of  $\text{WO}_3$  film as investigated by (a) grazing incidence X-ray diffraction and (b) Raman spectroscopy

To evaluate the photoelectrochemical performance of annealed  $\text{WO}_3$  thin films, the photocurrent responses were measured using an illuminating photoanode under solar light simulation. As exhibited in Figure 5(a), with the light switched on and off, the photocurrent response was improved in the case of annealed  $\text{WO}_3$  thin film while the as-deposited sample was inactive. For the high vacuum annealed  $\text{WO}_3$  photoanode, a nominal photocurrent could be observed at  $0.48 \mu\text{A}/\text{cm}^2$ . The air annealed condition exhibited the highest photocurrent of  $28.72 \mu\text{A}/\text{cm}^2$ . These phenomena can be attributed to the combining of the highest transparency and crystallinity of prepared sample. As transparency of film increases, more incident light can penetrate through the  $\text{WO}_3$  crystal structure. Therefore, more photo-excited carriers were created. During the electron transport process, the high crystallinity monoclinic phase of the air annealed sample facilitates electron transfer rate along the structure. In addition, the presence of an optimum amount of oxygen vacancies created in the air annealing treatment process acts as trap sites for electron-hole recombination. The higher photocurrent response was due to the combining of generation and separation of more photo-excited electron-hole pairs. The photocurrent response of the low vacuum annealed condition was reduced to  $3.46 \mu\text{A}/\text{cm}^2$ . This was due to favorable accumulation of  $\text{OH}^*$  species on the (200) plane [8]. These ion species obstruct photoactivity in the PEC water splitting, leading to a decrease in the photocurrent response. Furthermore, a high level of oxygen vacancies behaves as recombination center of photoelectron and hole; hence there is a reduction in the photo-water oxidation performance of the photoanode electrode. The transient spike can obviously be seen in the low vacuum annealed sample. This was due to the recombination of surface-trapped photo-generated minority carriers and the photo-generated major carriers [19]. Furthermore, the long-term stability of  $\text{WO}_3$  thin film annealed under air conditions was measured at 1800 s, as represented in Figure 5(b). It was observed that the photocurrent density that presented gradually decreased to about  $24.52 \mu\text{A}/\text{cm}^2$ . Nevertheless, good stability could be confirmed under the long-term irradiation.

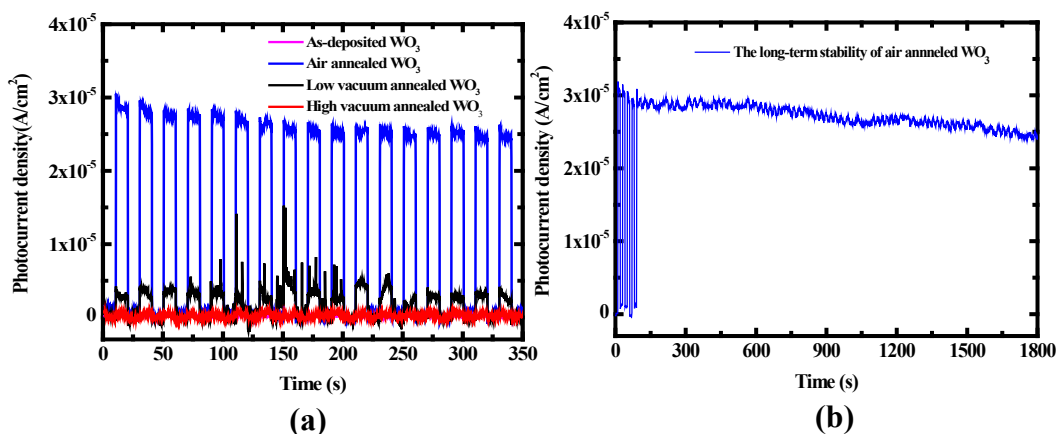


**Figure 5.** (a) Photo-current response and (b) long term stability of  $\text{WO}_3$  photoanode

#### 4. Conclusions

In this work,  $\text{WO}_3$  thin films for use as photo-anodes in PEC water splitting were synthesized by direct current magnetron sputtering. The prepared samples were treated under ambient air, high vacuum, and low vacuum annealing conditions at  $400^\circ\text{C}$ . The obtained results showed that suitable atmospheric annealing treatment improved the crystallinity and transparency of the samples. The air annealed samples exhibited the smallest thickness resulting in the achievement of the highest average transparency. It was clear that the air annealed sample promoted the most stable monoclinic phase, which occurred when an optimum level of oxygen vacancies was introduced into crystal structure. Hence, the air annealed  $\text{WO}_3$  thin film provided the highest photocurrent response at  $28.7 \mu\text{A}/\text{cm}^2$ . Additionally, this enhancement of photocurrent phenomena was due to a high transparency of thin film that encouraged the penetration of incident light photons throughout the crystal structure. In contrast, the photo-assisted water oxidation process of the low vacuum annealed sample was hindered by preferable accumulation of  $\text{OH}^*$  species on (200) plane, leading to a significantly reduced photocurrent response. Besides, a high abundance of oxygen vacancies activates the recombination process that diminishes the PEC water splitting rate. Therefore, the air annealed sample was the optimum photo-anode. It can be used in PEC water splitting applications that require a combination of high photo-excited carrier creation and high electron transport rate.

#### 5. Acknowledgements

This work was supported by National Science and Technology Development Agency (NSTDA), Thailand. We gratefully acknowledge Spectroscopic and Sensing Devices Research Group, National Electronics and Computer Technology Center (NECTEC) for instrument and financial support. The authors also appreciate the Advance Materials Design and Development (AMDD) Research Unit, Faculty of science and technology, Rajamangala University of Technology Thanyaburi, for performing the photoelectrochemical water splitting measurements.

## References

- [1] Wang, J., Ree, T., Wu, Y., Zhang, P. and Gao, L., 2018. Metal oxide semiconductors for solar water splitting. In: J.C. Védrine, ed. *Metal Oxides in Energy Technologies*. Amsterdam: Elsevier, pp.205-249.
- [2] Zong, X. and Li, C., 2018. Photocatalytic water splitting on metal oxide-based semiconductor photocatalysts. In: J.C. Védrine, ed. *Metal Oxides in Heterogeneous Catalysis*. Amsterdam: Elsevier, pp. 355-399.
- [3] Zheng, H., Ou, J., Strano, M.S., Kaner, R.B., Mitchell, A. and Kalantar-zadeh, K., 2011. Nanostructured Tungsten Oxide – Properties, Synthesis, and Applications. *Advanced Functional Materials*, 21(12), 2175-2196, DOI: 10.1002/adfm.201002477.
- [4] Liu, X., Wang, F. and Wang, Q., 2012. Nanostructure-based WO<sub>3</sub> photoanodes for photoelectrochemical water splitting. *Physical Chemistry Chemical Physics*, 14, 7894-7911, DOI: 10.1039/c2cp40976c.
- [5] Limwichean, S., Eiamchai, P., Ponchio, C. and Kasayapanand, N., 2021. Comparative investigations of DCMS/HiPIMS reactively sputtered WO<sub>3</sub> thin films for photo-electrochemical efficiency enhancements. *Vacuum*, 185(13), DOI: 10.1016/j.vacuum.2020.109978.
- [6] Limwichean, S., Kasayapanand, N., Ponchio, C., Nakajima, H., Patthanasettakul, V., Eiamchai, P., Meng, G. and Horprathum, M., 2021. Morphology-controlled fabrication of nanostructured WO<sub>3</sub> thin films by magnetron sputtering with glancing angle deposition for enhanced efficiency photo-electrochemical water splitting. *Ceramics International*, 47(24), 34455-34462, DOI: 10.1016/j.ceramint.2021.08.359.
- [7] Fernández-Domene, R.M., Roselló-Márquez, G., Sánchez-Tovar, R., Lucas-Granados, B. and García-Antón, J., 2019. Photoelectrochemical removal of chlorfenvinphos by using WO<sub>3</sub> nanorods: Influence of annealing temperature and operation pH. *Separation and Purification Technology*, 212, 458-464, DOI: 10.1016/j.seppur.2018.11.049.
- [8] Kalanur, S.S., Yoo, I., Cho, I. and Seo, H., 2019. Effect of oxygen vacancies on the band edge properties of WO<sub>3</sub> producing enhanced photocurrents. *Electrochimica Acta*, 296, 517-527, DOI: 10.1016/j.electacta.2018.11.061.
- [9] Mohamedkhair, A.K., Drmosh, Q.A., Qamar, M. and Yamani, Z.H., 2021. Tuning structural properties of WO<sub>3</sub> thin films for photoelectrocatalytic water oxidation. *Catalysts*, 11(3), DOI: 10.3390/catal11030381.
- [10] Chaiwas, S., Sakwan, P., Chananonwathorn, C., Hincheeranun, W., Horprathum, M. and Sangwaranatee, N., 2018. Effect of annealed ambient on structural, morphological and electrochromic properties of WO<sub>3</sub> nanoplates. *Suranaree Journal of Science and Technology*, 27(2), 1-5.
- [11] Limwichean, S., Eiamchai, P., Ponchio, C., Kasayapanand, N. and Horprathum, M., 2021. Comparative investigations of DCMS/HiPIMS reactively sputtered WO<sub>3</sub> thin films for photo-electrochemical efficiency enhancements. *Vacuum*, 185(13), DOI: 10.1016/j.vacuum.2020.109978.
- [12] Velevska, J., Stojanov, N., Pecovska-Gjorgjevich, M. and Najdoski, M., 2017. Electrochromism in tungsten oxide thin films prepared by chemical bath deposition. *Journal of Electrochemical Science and Engineering*, 7(1), 27-37, DOI: 10.5599/jese.357.
- [13] Xie, Y.P., Liu, G., Yin, L. and Cheng, H.-M., 2012. Crystal facet-dependent photocatalytic oxidation and reduction reactivity of monoclinic WO<sub>3</sub> for solar energy conversion. *Journal of Materials Chemistry*, 22(14), 6746-6751, DOI: 10.1039/C2JM16178H.
- [14] Danial, M.F., Desbat, B., Lassegues, J.C., Gerand, B. and Figlarz, M., 1987. Infrared and Raman study of WO<sub>3</sub> tungsten trioxides and WO<sub>3</sub>·xH<sub>2</sub>O tungsten trioxide hydrates. *Journal of Solid State Chemistry*, 67, 235-247, DOI: 10.1016/0022-4596(87)90359-8.
- [15] Trasferetti, B.C., Rouxinol, F.P., Gelamo, R.V., de Moraes, M.A.B. and de Faria M.A.B., 2004. Berreman effect in amorphous and crystalline WO<sub>3</sub> thin films. *The Journal of Physical Chemistry B*, 108(33), 12333-12338, DOI: 10.1021/jp036653u.

- [16] Djaoued, Y., Balaji, S. and Bruning, R., 2012. Electrochromic devices based on porous tungsten oxide thin films. *Journal of Nanomaterials*, 2012(2), DOI: 10.1155/2012/674168.
- [17] Zhang, W., Fan, Y., Yuan, T., Lu, B., Liu, Y., Li, Z., Li, G., Cheng, Z. and Xu, J., 2020. Ultrafine tungsten oxide nanowires: synthesis and highly selective acetone sensing and mechanism analysis. *ACS Applied Materials and Interfaces*, 12(3), 3755-3763, DOI: 10.1021/acsami.9b19706.
- [18] Roselló-Márquez, G., Fernández-Domene, R.M., Sánchez-Tovar, R. and García-Antón, J., 2020. Influence of annealing conditions on the photoelectrocatalytic performance of WO<sub>3</sub> nanostructures. *Separation and Purification Technology*, 238(9), DOI: 10.1016/j.seppur.2019.116417.
- [19] Wang, D., Bassi, P.S., Qi, H., Zhao, X., Gurudayal, Wong, L.H., Xu, R., Sritharan, T. and Chen, Z., 2016. Improved charge separation in WO<sub>3</sub>/CuWO<sub>4</sub> composite photoanodes for photoelectrochemical water oxidation. *Materials*, 9(5), DOI: 10.3390/ma9050348.